INSTITUT DE FRANCE
Académie des sciences

Comptes Rendus
Mécanique

Ilige S. Hage and Ramsey F. Hamade

Experimentally validated combined stiffness expression for finite domain containing multiple inclusions

Volume 348, issue 2 (2020), p. 113-135

Published online: 24 June 2020

https://doi.org/10.5802/crmeca.11

Les Comptes Rendus. Mécanique *sont membres du Centre Mersenne pour l'édition scientifique ouverte*
www.centre-mersenne.org
e-ISSN : 1873-7234

Comptes Rendus
Mécanique
2020, 348, nº 2, p. 113-135
https://doi.org/10.5802/crmeca.11

Experimentally validated combined stiffness expression for finite domain containing multiple inclusions

Ilige S. Hage [a] **and Ramsey F. Hamade** *, [b]

[a] Department of Mechanical Engineering, Notre Dame University-Louaize, Zouk Mosbeh, P.O.Box: 72, Zouk Mikael, Lebanon

[b] Department of Mechanical Engineering, American University of Beirut, Riad El-Solh, Beirut 1107 2020, Lebanon.

E-mails: ilige.hage@ndu.edu.lb (I. S. Hage), rh13@aub.edu.lb (R. F. Hamade).

Abstract. Traditional homogenization formulations for finite volume are extended to allow for the consideration of multiple inclusions and their spatial distributions along with their corresponding individual geometric attributes. For all inclusions present in different states, a combined homogenization formulation (dubbed generalized stiffness formulation, GSF) is posed for summing the five geometric attributes of volume fraction (VF), shape or aspect ratio (AR), orientation, location (position within the domain), and number of inclusions in the domain. For verification, the solutions are compared to two literature-reported calculations of simple cases of domains containing one inclusion of specific shape and orientation in which only one attribute is varied. Once verified for simple cases, GSF stiffness solutions were run for 5040 cases of domains containing multi inclusions with various configuration combinations. These solutions were compared against 36 identical cases of 3-dimensional (3D) domains printed using acrylonitrile butadiene styrene (ABS) and experimentally tested under mechanical compression. Additionally, finite element method (FEM) simulations are run of these test structures under compression. For these test cases, effective composite stiffness values are compared for numerical solutions, experimental tests, and FEM. Relative effects on stiffness of the five inclusion geometric attributes are assessed.

Keywords. Composite homogenization, Stiffness formulation, Multiple inclusions.

Manuscript received 3rd December 2019, revised 30th January 2020, accepted 16th March 2020.

1. Introduction

The presence of porosities in solids punctuates many technical materials both natural and synthetic alike. In most practical cases, porosity presents itself in randomly shaped and distributed inclusions or voids. Quantifying the combined effect of such inclusions has been at the heart of mechanics in dealing with how to "homogenize" such materials. Much of the reported work on

* Corresponding author.

composites containing single and multiple inclusions of various types is based on the original work to determine the elastic field of ellipsoidal inclusion of Eshelby [1] and on the later work of Mori and Tanaka [2]. While the interior Eshelby tensor is constant with respect to the inclusion position, the interior Eshelby tensor is function of the matrix Poisson's ratio, shape, and orientation. The exterior Eshelby tensor is function of the matrix Poisson's ratio and the inclusion's shape, orientation, and position. Reported works (e.g., [3–7], and [8]) have found solutions for interior and exterior components of the Eshelby tensor for a single (mostly ellipsoidal) inclusion taking into account the effect of its volume fraction, orientation, and shape based on the work of Mori–Tanaka [2]. Such works do not account for the effects of the multiple inclusions' positional distribution within the medium nor for the number of these inclusions. Rather than consider only one inclusion's volume fraction or shape at a time as done in conventional homogenization analyses, this work accounts for the composite stiffness of a finite domain with multiple ellipsoidal inclusions.

This work is devoted to validating a new homogenization method for linear elastic composite materials by comparing the resulting estimate of the overall stiffness to estimates produced by finite element computations and also to strain measurements utilizing 3D-printed microstructures. This homogenization scheme of multi inclusions is an extension of recent work by the authors (Hage and Hamade, [9]) that calculates the stiffness of a domain containing a single inclusion with its corresponding shape, volume fraction, and orientation. The work is based in part on the superposition of strain field principle as described by Li *et al.* [10] that considers one inclusion in finite and infinite domains (without accounting for location) and also expands on the works of Ju and Sun [11–13]. The concept of superposition of strain field was used by Askari *et al.* [14] for modeling of inclusions and precipitation hardening in metal matrix composites. This work advances a combined formulation for the effective stiffness tensor of a finite domain while considering the combined effects of multiple ellipsoidal inclusion's attributes: volume fraction, VF, aspect ratio (accounted for via the Eshelby tensor expression), AR, location (position), r, and 3D orientation (via angles θ, φ, γ, where the inclusions are voids. The scheme relies on the average stress consistency condition introduced by (Li *et al.* [10]) that does not require a balanced stress whenever the Eshelby tensor becomes non-uniform on the ellipsoidal inclusion. This situation occurs as soon as a finite domain is considered in Eshelby's problem, and this situation is at the heart of the present study aiming at accounting for boundary effects. Indeed, in the case of an infinite matrix, the new estimate is perfectly identical to the one of Mori–Tanaka, which is also observed by comparing the new estimate to the one of Mori–Tanaka on configurations taken from the literature. Since the formulation of the stiffness tensor in Li *et al.* [10] takes into account only one inclusion and only one parameter (i.e., volume fraction), the was further verified here against similar cases to those of Mori–Tanaka's and taking only this one parameter. Also considered in this work the effect of multiple inclusions within the same representative volume element (RVE) by estimating the combined effect of each individual inclusion on the strain field for the composite as the summed effect of all inclusions (interior and exterior strains) within the RVE is calculated. An expression is developed based on a modified Mori–Tanaka method combined with the dual-eigenstrain (interior and exterior eigenstrain) method. From the dual eigenstrain method, an Eshelby tensor, dependent on the inclusion's shape and position, is deduced. Employing the strain field superposition principle, this is applied for multiple inclusions considering all the above variables into one formulation. A global coordinate system for the composite is adopted at its center, and the position of each inclusion is formulated and re-oriented using 3D transformation matrices with respect to this global system. The orientation of each inclusion is taken into account by multiplying the strain concentration tensors with a transformation tensor function of the 3D transformation matrices. The resulting formulation yields a compact expression so that effective composite stiffness may be determined for any number of inclusions with

combinations of geometric (ellipsoidal) attributes of a composite containing multiple inclusions. These formulations are reported in Section 2.

A numerical validation section (Section 3) is included as a numerical validation of GSF stiffness solutions as compared with literature solutions. Thus, this work findings are applicable to combinations of variables that are not covered in other techniques based on Mori–Tanaka. Previous works are applicable in cases where one should fix one of the variables (position, shape, volume fraction, orientation, or number of inclusions). However, this work takes into account the combined effect of all these variables. This formulation's numerical estimates of stiffness are compared to simpler cases reported in the literature: cases with specific shapes and orientations of single inclusion in which one variable (e.g. inclusions position, shape, volume fraction, orientation, and number of inclusions) is fixed. Simple inclusion cases are considered that account only for one variable at a time and omitting the effect of location and number of inclusions, this work's estimates mimic those of the simplified Mori–Tanaka scheme. This accomplishment represents verification to literature-reported results using Mori–Tanaka scheme. The section contains one verified case of stiffness variation with inclusions volume fraction and another with shape (aspect ratio).

Furthermore, extensive experimental verification is employed (Section 4) to validate the formulations numerical solutions where a novel method is employed via compression tests of 3D printed cubes. Numerous cases that present many dramatically representative combinations of multiple inclusions are considered. Combinations of multiple inclusions with different variables and levels: volume fraction (0, 0.05, 0.1, 0.2, 0.25, 0.3, 0.35, 0.4, 0.5, 0.6, 0.7, 0.8, 0.9, 1), shapes (aspect ratios 0.1, 0.2, 0.3, 0.4, 0.5, 0.55, 0.65, 0.7, 0.75, 0.8, 0.9, 1, 1.25), orientations (0°, 15°, 30°, 45°, 60°, 75°, 90°), locations (Agglomerated (centered) versus dispersed (at the corners)), and number of inclusions (1, 4, 8, 16, 32, 64) were modeled on CAD according to a DOE test matrix, printed, and compression tested. In Section 5, finite element method (FEM) simulations of these cases are also run for further corroboration. Section 6 reviews and compares the numerical stiffness results to experimentally found values and to FEM results.

To its credit, the scheme accounts for the combined effect of inclusions' positions, shapes, volume fractions, orientations, and number. The formulation is also customizable for finite or infinite domains. In addition, it is able to handle multiple numbers of inclusions with specified locations, orientations, volume fractions and aspect ratios. This aspect is crucial in the field of composites where, not only simple cases, but randomly located cases of inclusions with various aspect ratios must be dealt with.

2. Homogenization formulation for multiple inclusions

In this section, the application of the strain field superposition principle is delineated. To account for multiple inclusions' 3D orientations and locations within the RVE, the effect of each individual inclusion is estimated w.r.t. the RVE Cartesian coordinate using translation and rotation transformation matrix.

2.1. *Transformation from local to global coordinates*

In order to account for the effect of multiple inclusions and their orientations, a representative volume element (RVE) with its corresponding Cartesian coordinate system is shown in Figure 1. Also shown in the 3D RVE are inclusions distributed with multiple orientations with their corresponding rotation angles identified with respect to the RVE Cartesian coordinate. To move from each inclusion's local coordinate system to the global RVE coordinate system, a transformation matrix is utilized to account for the orientation of each individual inclusion within the RVE (Hage

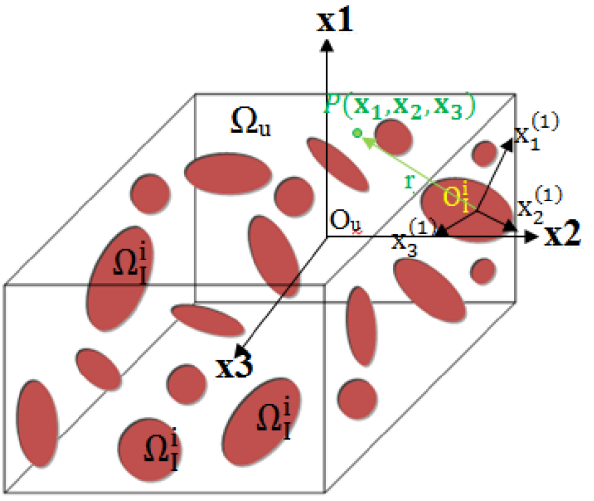

Figure 1. Illustration of a finite domain (and its global coordinate system) multiple ellipsoidal inclusions (with their local coordinate systems).

and Hamade, [9]). The composite is considered as domain Ωu having multiple inclusions Ω_I^i from $i = 1, \ldots, N$ (where N is the total number of inclusions). Figure 1 is an illustration of such a finite domain with multi ellipsoid inclusions. Shown is the composite domain (and its global coordinate system) with mix of multiple inclusions and various attributes (with their local coordinate systems). The origin, Ou, of the coordinate system is set at the center of the domain. The origin of each inclusion domain Ω_I^i is noted as O_I^i ($x^{(1)} = (x_1^{(1)}, x_2^{(1)}, x_3^{(1)})$) where (1) refers to the considered inclusion (for the sake of non-confusion "(1)" is used for the considered inclusion and "i" is used for the studied point P). The coordinates $(x_1^{(1)}, x_2^{(1)}, x_3^{(1)})$ for the origin of each inclusion are obtained with respect to the origin of the composite domain coordinate system. Using the transformation matrix and considering that r is the distance between point P in the domain and the origin of the considered inclusion, the coordinate position vector is reoriented to the inclusion coordinate system and reformulated in the composite domain (Hage and Hamade, [9])

$$\begin{bmatrix} x_1 \\ x_2 \\ x_3 \end{bmatrix} = Q_{ij} \left(\begin{bmatrix} {x_1}^i \\ {x_2}^i \\ {x_3}^i \end{bmatrix} - \begin{bmatrix} x_1^{(1)} \\ x_2^{(1)} \\ x_3^{(1)} \end{bmatrix} \right) \tag{1}$$

where $\begin{bmatrix} {x_1}^i \\ {x_2}^i \\ {x_3}^i \end{bmatrix}$ refers to the coordiantes of any point P in the space

$$r = \sqrt[2]{((x_1)^2 + (x_2)^2 + (x_3)^2)} \tag{2}$$

In addition, Q_{ij} is a transformation matrix is utilized to account for the orientation of the inclusion within the 3D RVE and is utilized to jump from the inclusion local coordinate system to the global RVE coordinate system [9].

This reformulated coordinate position distance r is used to determine the exterior Eshelby tensor and is function of the orientation and coordinates of the center of each inclusion w.r.t. the origin of the domain, $r = f(\theta, \varphi, \gamma, O_I^i)$.

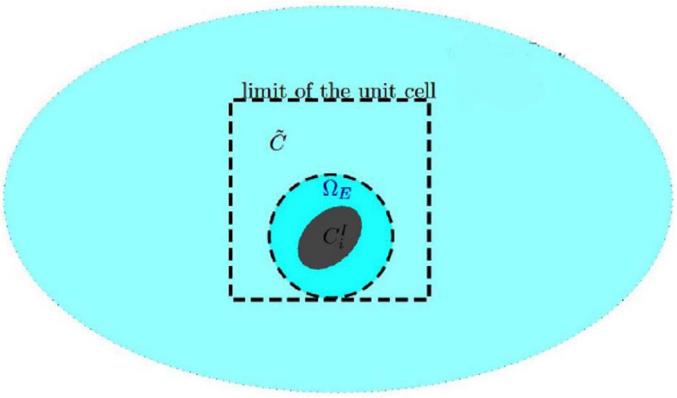

Figure 2. The composite domain of the inclusion inside the exterior cube domain.

2.2. *Effective stiffness tensor: generalized stiffness formulation*

The effective stiffness tensor of a composite with multiple inclusions is calculated based on the superposition principle of strain fields (Li *et al.*, [10]). The effect of the boundary conditions on the inclusion is taken into account by the position factor and the distance between the boundary and the inclusion, which is added as a variable. The authors examined two cases: one in which inclusions are located near the center of the RVE and another case where inclusions are closer to the boundary of the RVE. Although the code allows for ellipsoidal or spherical shaped RVEs, reported in this work is a finite cube-shaped RVE. Cluster of inclusions is inserted into the finite RVE. The Matlab® code checks whether inclusions satisfy the condition of being fully contained within RVE.

At the inner side of the RVE, the elastic field strain is divided into two fields: one from the background (external boundary loads) and another due to the presence of the inclusion field [10]. The new average strain in each phase is the sum of the background strain and the disturbance strain. The averaged interior and exterior Eshelby tensors (being key for determining the elastic field of an ellipsoidal inclusion interiorly and exteriorly) for each inclusion are summed.

In this work, each inclusion is treated as a subdomain within an infinite domain where a stress-free eigenstrain is prescribed in the inclusion and vanishes outside. Since multiple inclusions are considered inside the bounded RVE, the inclusion inside the cube is a finite domain and the exterior Eshelby is calculated between the inclusion and its boundary as can be shown in Figure 2 where $\tilde{C}$ is the reference solid stiffness tensor and C_i^I is the stiffness tensor of each inclusion, Ω_{E} is the exterior domain of the inclusion used to calculate the strain field outside the inclusion domain, and the dashed circle corresponds to the shape of the inclusion domain which could be elliptical (or spherical, a special case).

The Eshelby tensor for one inclusion is calculated using the summation of the interior classical Eshelby tensor (adapting the formulation by Mura [15]) and exterior Eshelby function of the position x (using the formulation by Ju *et al.* [11]). These formulations related to the Eshelby tensor are based on two components: one is uniform but a function of the matrix Poisson's ratio, shape, and orientation and is constant with position and the other is a function of the matrix Poisson's ratio, shape, orientation, and the re-oriented coordinate vector position.

Translating the effective stiffness tensor into the global domain, the strain concentration tensors for each inclusion A^E, and A^I is calculated in the local domain and equivalent strain concentration tensors are calculated in the global system using a 4th rank transformation tenor, Q_{ijkl} (Koay [16], this tensor is function of the transformation matrix Q_{ij} [9] defined in the

previous section). The "Bond transformation" [17] is a tensor that accounts for the inclusion's 3-dimensional attributes.

The derived expression for the effective stiffness tensor for multiple inclusions reported by Li *et al.* [10] and Hage and Hamade [9] becomes

$$\overline{C} = \left[\sum_{i=1}^{N} f_i * C_i^I : Q_{ijkl} : A_i^E + \left(1 - \sum_{i=1}^{N} f_i\right) \sum_{i=1}^{N} C^E : Q_{ijkl} : A_i^I\right] : \left[\sum_{i=1}^{N} f_i * Q_{ijkl} : A_i^E + \left(1 - \sum_{i=1}^{N} f_i\right) \sum_{i=1}^{N} Q_{ijkl} : A_i^I\right]^{-1} \tag{3}$$

where

$$\begin{aligned} A_i^E &= I^s - \tilde{C}_i^{-1} : (\tilde{C}_i - C^E) : \Delta S^* \\ &= I^s - [aC_i^I + (1-a)C^E]^{-1} : (aC_i^I + (1-a)C^E - C^E) : \langle S_i^{I,*}(\tilde{C}_i, f = f_i)\rangle_{\Omega_I} \\ &\quad - \langle S_i^{E,*}(\tilde{C}_i, f = f_i)\rangle_{\Omega_E} \\ A_i^I &= I^s - \tilde{C}_i^{-1} : (\tilde{C}_i - C_i^I) : \Delta S^* \\ &= I^s - [aC_i^I + (1-a)C^E]^{-1} : (aC_i^I + (1-a)C^E - C_i^I) : \langle S_i^{I,*}(\tilde{C}_i, f = f_i)\rangle_{\Omega_I} \\ &\quad - \langle S_i^{E,*}(\tilde{C}_i, f = f_i)\rangle_{\Omega_E} \end{aligned}$$

Note that

$$\langle \cdots \rangle_{\Omega_u} = \frac{1}{|\Omega_u|} \int_{\Omega_u} \ldots \mathrm{d}\Omega_u$$

where

i	inclusion number
$\overline{C}$	effective stiffness tensor of the composite
f_i	volume fraction of each inclusion
C_i^I	stiffness tensor of the each inclusion
C^E	stiffness tensor of the matrix
A_i^E	exterior strain concentration tensor for each inclusion (Li *et al.* [10])
A_i^I	interior strain concentration tensor for each inclusion (Li *et al.* [10])
$\tilde{C}_i$	reference solid stiffness tensor (function of the inclusion and matrix stiffness tensors) calculated for each inclusion (Li *et al.* [10]), $\tilde{C}_i = aC_i^I + (1-a)C^E, 0 \le a \le 1$
I^s	identity tensor
$S_i^{I,*}/S_i^{E,*}$	interior and exterior Eshelby tensors calculated for each inclusion (Mura [15] and Ju and Sun [11])
Q_{ijkl}	rotation tensor function of Q_{ij} as defined in [9].

In (3), both A_i^E and A_i^I as shown are function of averaged interior and exterior Eshelby tensor $S(r)$ (these tensors are function of ν_m is the Poisson ratio of the matrix, α is the aspect ratio of the inclusion and the position of the inclusions r) and the stiffness tensors fo the matrix, C^E, and inclusions C_i^I and the reference solid stiffness tensor $\tilde{C}_i = aC_i^I + (1-a)C^E$ for each inclusion thus A_i^E and its complex relation with all the aforementioned variables could be simplified as a function named herein by "g" as follows $A_i^E = g(S(r), \tilde{C}_i, C^E, C_i^I)$ same stands for $A_i^I = g'(S(r), \tilde{C}_i, C^E, C_i^I)$. Given $r = f(\theta, \varphi, \gamma, \mathrm{O}_D^n)$, the effective stiffness tensor is function of all 5 considered inclusions attributes: volume fraction (f), aspect ratio (α evaluated in $S(r)$, orientation (evaluated in r and using Q_{ijkl}), locations (r), and number of inclusions (averaging over multiple inclusion by using the principle of superposition of strain fields and summing for $i = 1$ to N). As "a" is a parameter used to describe the comparison solid, it has to be chosen either to yield $\tilde{C} = C^E$ or $\tilde{C} = C^I$ where the method would degenerate either to interior homogenization or the exterior homogenization, respectively. In this work, the parameter "a" is set to 0.01 thus

favoring the exterior finite RVE. This value was chosen in order to take into account the effect of all the inclusions on each other inside the exterior cubic RVE without neglecting the effect of each inclusion with respect to its interior domain. It was so chosen to lie in between these two special cases (exterior and interior).

Using Matlab®, the inverse tensors are calculated. Based on the component's inverse matrices, an extension formulation of Li *et al.* [10] is the aggregate stiffness formulation becomes:

$$\begin{aligned}\overline{C} = &\left[\sum_{i=1}^{N} f_i * C_i^I : g[S(f(\theta,\varphi,\gamma,O_D^n)), \tilde{C}_i, C^E, C_i^I]\right. \\ &+ \left.\left(1-\sum_{i=1}^{N} f_i\right)\sum_{i=1}^{N} C^E : g'[S(f(\theta,\varphi,\gamma,O_D^n)r), \tilde{C}_i, C^E, C_i^I]\right] : \left[\sum_{i=1}^{N} f_i * g[S(f(\theta,\varphi,\gamma,O_D^n)), \tilde{C}_i, C^E, C_i^I]\right. \\ &+ \left.\left(1-\sum_{i=1}^{N} f_i\right)\sum_{i=1}^{N} g'[S(f(\theta,\varphi,\gamma,O_D^n)), \tilde{C}_i, C^E, C_i^I]\right]^{-1} \end{aligned} \tag{4}$$

Based on strain field superposition (summation) of each inclusion, Equation (4) incorporates the aggregate effects of multi inclusions including location/distribution within the medium. In addition to the 3 classical variables of volume fraction, shape, and orientation, this formulation accounts for the additional effects of 2 additional variables: number count and locations of inclusions.

Most homogenization literature report on calculations of stiffness as function of inclusions' volume fraction and shape considering either uniform orientation or random orientations. To the best of the author's knowledge, no other reported work takes into account the combined effects of all 5 parameters (volume fraction, shape, orientation, location, and number) at the same time in one formulation with a range of variation for each parameter. This GSF work accomplishes this by extending the original formulations by Li *et al.* [10] to include the effects of inclusions'

(1) Orientations: orientations were never taken as a parameter with a level range as in this work

(2) Locations: while formulating the exterior point Eshelby's tensor of an ellipsoidal inclusion. To account for this parameter, works in [11] and [15] were combined. Considering the concept of superposition of strain fields (interior and exterior Eshelby and the interaction with multiple inclusions) which has never been reported before

(3) Inclusions' number by taking the interaction of the strain field for multiple inclusions.

Noting that the superposition assumptions was based on calculating the interior and exterior Eshelby tensors/eigenstrain method where the exterior tensors are function of the position of the inclusions in the domain and there is no restriction regarding the positions of the inclusions in calculating the exterior tensors, the tensor could be calculated for any position, thus it was assumed that the superposition of strain field or in other words overlapping of strain fields is applicable at any position.

Comparing (3) and (4) with the work done in [10], one can see the added terms of (1) the summation of strain fields due to the effect of multiple (N) inclusions in one matrix thus the effect of location is taken into account in this term inside the new Eshelby tensor dependent on r the inclusions' locations, (2) the effect of the inclusion orientation in the Q tensor. One contribution of this work is to add in one formulation (dubbed GSF) the effect of the inclusions' number, location, orientation, volume fraction and shape, which is a novelty to the field of composites homogenization. This GSF enhanced formulation, takes into consideration anisotropic composites, due to the added terms of inclusions' multiple shapes and orientations which makes the composite anisotropic in nature, and thus the authors will verify this formulation later on in this paper to 3D printed ABS plastics which are not isotropic, and prove the validity of GSF to anisotropic composites.

3. Solutions

In this section, the numerical solution of (3) and (4) are validated for 2 cases reported in the literature. The homogenization scheme in this work is a generalized method customizable to finite and infinite domains and may be applied to particular cases with same assumptions as in Mori–Tanaka. The comparisons below validate the notion that (3) and (4) yield comparable results to those of Mori–Tanaka in which one of the 5 variables (inclusion position, shape, volume fraction, orientation, and number) is fixed. While classical homogenization methods can be applied for cases where the number of inclusions is larger than 10, GSF could be used for any number of inclusions.

3.1. *Volume fraction validation*

This case compares GSF calculations of normalized Young's modulus values versus volume fraction of porosity values obtained from the homogenization work reported by Dai *et al.* [18] for 3-phase composite containing a centered spherical inclusion (Zener anisotropic ratio = 1). Each constituent is elastic and isotropic.

The spatial locations of the inclusions are arranged in such way that the composite is isotropically homogeneous (thus $E_{11} = E_{22} = E_{33} = E$) with material properties:

- Epoxy matrix with $E_0 = 2.03$ GPa and $\nu_0 = 0.40$
- First inclusion phase (quartz) with $E_1 = 73.6$ GPa and $\nu_1 = 0.25$
- Second inclusion phase (void) with $E_2 = 0$
- The volume fraction $c1$ of quartz-sand is related to the void volume fraction $c2$ by $c1 = 0.17(1 - c2)$. This equation allows to have a variety of composites, for example if $c2 = 0$ this means the composite has only the quartz inclusion with a volume fraction of 0.17. When $c2 = 1$, this means that the composite is fully a void (not a realistic case), and when $0 < c2 < 1$ this means $0.17 > c1 > 0$, and the composite is comprised of both a void and a quartz inclusion with different volume fractions. (When $c2$ (the volume fraction of the void) = 0 this means $c1$ (the volume fraction of the quartz) = 0.17 thus the composite is comprised of the Epoxy matrix and one quartz inclusion harder than the matrix thus the composite will have a modulus higher than that of the matrix which means that $E_{\text{composite}}/E_0$(modulus of the matrix = 2.03) = $E/E_0 > 1$ equal to 1.4 based on M-T and GSF.)

Figure 3 shows good agreement between the numerical results of the GSF homogenization method (4) with those reported by Dai *et al.* [18].

3.2. *Shape validation*

Rouhi and Rais-Rohani [19] reported on the general framework of modeling the stiffness properties of carbon nano-fibers enhanced composite materials. A nano-enhanced matrix with CNF as the reinforcement material and vinyl ester resin as the matrix having the following elastic properties: $E_0 = 3.5$ GPa, $E_1 = 450$ GPa, and $\nu_0 = \nu_1 = 0.3$. Figure 4 represents the axial Young's modulus with respect to the elliptical aspect ratio of the inclusion obtained using the developed homogenization code in comparison with the published results.

4. Validation of the generalized stiffness formulation: experimental compression testing and fem of domain cubes containing multiple inclusions

In Mori–Tanaka, one inclusion variable (e.g., inclusion position, shape, volume fraction, orientation and number) has to be fixed. The scheme in this work is presented as capable of addressing

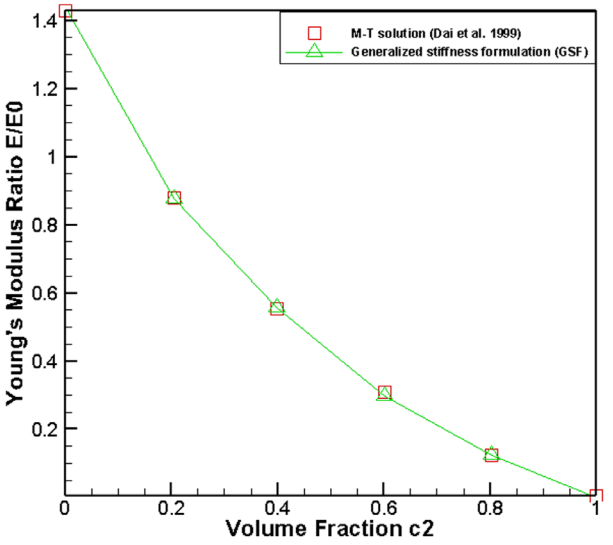

Figure 3. Comparison of the numerical results using this work's homogenization method versus results reported in [18].

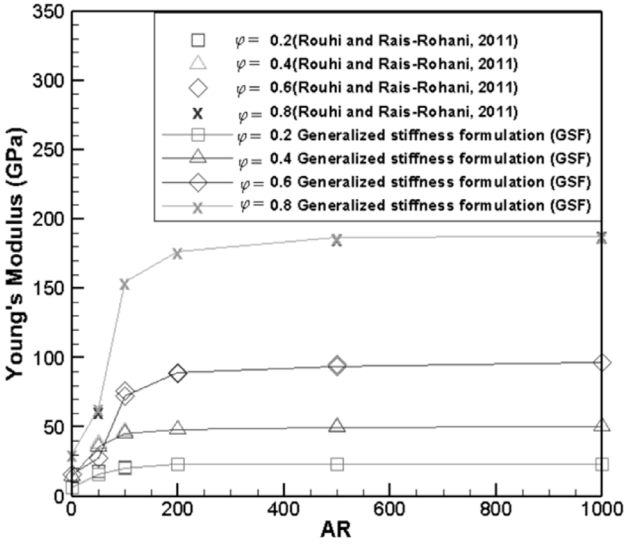

Figure 4. Comparison of the numerical results using the developed homogenization method with results reported by Rouhi and Rais-Rohani [19]).

any number and combination of inclusion states. In this Section, the scheme will be validated for finite domains where novelty is claimed at the expense of relying on the "average stress consistency condition" of Li *et al.* [10]. Corroboration is performed by comparing against compression experiments on 3D printed composite specimens containing multiple inclusions and by the finite element method (FEM). This section reports on the design, details, and results of the performed experimental compression tests.

Table 1. DOE Multi inclusion test matrix: variables and levels

Variable		Levels
1. Volume fraction	14	0, 0.05, 0.1, 0.2, 0.25, 0.3, 0.35, 0.4, 0.5, 0.6, 0.7, 0.8, 0.9, 1
2. Shape (aspect ratio)	13	0.1, 0.2, 0.3, 0.4, 0.5, 0.55, 0.65, 0.7, 0.75, 0.8, 0.9, 1, 1.25
3. Orientation	7	0°, 15°, 30°, 45°, 60°, 75°, 90°
4. Location	2	Agglomerated (centered), Dispersed (at the corners)
5. Number of inclusions	6	1, 4, 8, 16, 32, 64

Table 2. Multi inclusion cases with prescribed levels for the 4 quantitative variables tested analytically

Number of inclusions	Size (volume fraction)	Shape (aspect ratio)	Orientation
1, 4, 8, 16, 32, 64 (420 ∗ 6)	0.05	0.1, 0.2, 0.3, 0.4, 0.5, 0.55, 0.65, 0.7, 0.75, 0.8, 0.9, 1, 1.25	0°, 15°, 30°, 45°, 60°, 75°, 90°
	0.1	0.2, 0.3, 0.4, 0.5, 0.55, 0.65, 0.7, 0.75, 0.8, 0.9, 1, 1.25	0°, 15°, 30°, 45°, 60°, 75°, 90°
	0.2	0.4, 0.5, 0.55, 0.65, 0.7, 0.75, 0.8, 0.9, 1, 1.25	0°, 15°, 30°, 45°, 60°, 75°, 90°
	0.25	0.5, 0.55, 0.65, 0.7, 0.75, 0.8, 0.9, 1, 1.25	0°, 15°, 30°, 45°, 60°, 75°, 90°
	0.3	0.65, 0.7, 0.75, 0.8, 0.9, 1, 1.25	0°, 15°, 30°, 45°, 60°, 75°, 90°
	0.35	0.7, 0.75, 0.8, 0.9, 1	0°, 15°, 30°, 45°, 60°, 75°, 90°
	0.4	0.8, 0.9, 1	0°, 15°, 30°, 45°, 60°, 75°, 90°
	0.5	1	0°, 15°, 30°, 45°, 60°, 75°, 90°

4.1. *Design of experiments of finite domain with multiple inclusions*

Several composites are designed using design of experiment (DOE) SAS/JMP® software to determine the effect on the effective Young's modulus of the composite of inclusions' volume fractions, shapes, orientations, numbers, and locations within the matrix. Full factorial DOE is utilized with 5 considered variables and their value ranges as listed in Table 1.

"Agglomerated" locations refer to inclusions are positioned near the center of the cube while and "dispersed" represents inclusions that are far away from the center and nearby the walls of the cube. These positions are chosen to cover 2 extreme cases of inclusions locations within the cubical RVE to reveal whether there is an effect of locations.

In full-factorial experiments, the number of experiments required is $13 * 6 * 14 * 7 * 2 = 15288$ cases. Excluding cases where inclusions protrude outside the composite domain of the cube or overlap with other inclusions reduces this number. The cases that satisfy this condition are listed in Table 2. These cases are tested for two schemes for inclusion distribution: 2520 agglomerated inclusions case and 2520 evenly dispersed inclusions cases for a total number of 5040 cases.

Table 3. Experimental cases printed on the 3D printed cubes

Experiment total number	Number of inclusions and shapes	Orientation	Location	VF
5	8 spheres	0°	agglomerated	0.05–0.1–0.2–0.25–0.3
5	8 ellipses	0°	agglomerated	0.05–0.1–0.15–0.2–0.25
5	8 spheres	0°	dispersed	0.05–0.1–0.2–0.25–0.3
5	8 ellipses	0°	dispersed	0.05–0.1–0.15–0.2–0.25
2	8 ellipses	90°	agglomerated	0.1–0.2
2	8 ellipses	90°	dispersed	0.1–0.2
2	8 ellipses	random	agglomerated	0.1–0.2
2	8 ellipses	random	dispersed	0.1–0.2
1	1 sphere	0°	centered	0.2
1	16 spheres	0°	dispersed	0.2
2	2 spheres–6 ellipses	0°	dispersed	0.1–0.2
2	4 spheres–4 ellipses	0°	dispersed	0.1–0.2
2	6 spheres–2 ellipses	0°	dispersed	0.1–0.2

4.2. *3D printing of domain cubes containing multiple inclusions*

In order to generate test specimens with predefined inclusion's volume fraction, aspect ratio, orientation, number, and location, 3D printing technology has been adopted using a second-generation cube 3D printer (Cubify, Cube 3D Printer 2nd Generation: printer model number: 381000) and using ABS plastic filament (product number CC3D2 GEN-ABS). A subset of the cases listed in Table 2 are 3D-printed, experimentally tested, and modeled using FEM. Taguchi's orthogonal arrays full factorial is utilized with 5 variables:

- Shape variable with 2 levels: spheres (AR = 1) and elliptical inclusions (AR = 1.25).
- Position variable with 2 levels: dispersed and agglomerated inclusions.
- Volume fraction variable with 3 levels: 0.05, 0.1, 0.2, 0.25, 0.3 for the spheres; and 0.05, 0.1, 0.15, 0.2, 0.25 for the ellipses.
- Orientation variable with 3 levels: 0°, 90° and random orientation.
- Number of inclusions variable with 3 levels: 1, 8, 16 spheres.

The number of experiments was reduced due to the deletion of repeated or redundant cases. Additional reductions were required due to practical (printing) reasons where the aspect ratios of interest were limited to a range of 1–1.25. Therefore, the scheme is currently limited to spherical and elliptical inclusions but remains untested in the case of flat and elongated inclusions. Consequently, the number of test cases was reduced to the 36 cases listed in Table 3.

The effect of number of inclusions is taken into account via 3 experiments all at VF = 0.1: (1) 2 spheres and 6 ellipses with dispersed positions, (2) 4 spheres and 4 ellipses with dispersed positions, and (3) 6 spheres and 2 ellipses with dispersed positions, with ellipses at 0° orientation. The effect of inclusions shape (calculated as % circular or % elliptical inclusions) is also considered.

For all cases, the finite domain is taken as uniform with cubic dimensions of $16 * 16 * 16$ mm^3. The composite has a matrix composed of ABS plastic shaped by fusing filament wire in a 3D printing apparatus. Using Cubify Design® software, the cases listed above are designed to generate *.stl files with dimensional tolerance of 0.001 mm. The dimensions of the spheres and ellipses inclusions are designed to have the predefined volume fractions and aspect ratios for all 36 cases.

Figure 5 summarizes the designed composites along with photographs of sectioned cubes showing horizontal sections in (x, y) plane: 8 spheres dispersed, 8 spheres agglomerated, 8 ellipses dispersed at 0° with z-axis, 8 ellipses agglomerated at 0° with z-axis, 8 ellipses dispersed at 90° with z-axis, 8 ellipses agglomerated at 90° with z-axis, 8 ellipses dispersed at random orientation with z-axis, 8 ellipses agglomerated at random orientation with z-axis, 2 spheres and 6 ellipses, 4 spheres and 4 ellipses, 6 spheres and 2 ellipses, 1 sphere at VF = 0.2, 8 spheres at VF = 0.2 with random positions, 16 spheres at VF = 0.2 with random positions. The dimensions of the spheres and ellipse inclusions are so chosen as to yield predefined volume fraction as follows:

For the 8 spheres the diameter of the spheres $D = 4.6$ mm at VF = 0.1, $D = 5.8$ mm at VF = 0.2 and $D = 6.6$ mm at VF = 0.3.

For the 8 ellipses the major axis length $a = 5.36$ mm, minor axis length $b = 4.288$ mm, the third axis is considered to be equal to the minor axis $c = b = 4.288$ mm at VF = 0.1; $a = 6.12$ mm, $b = c = 4.896$ mm at VF = 0.15; and $a = 6.7$ mm, $b = c = 5.36$ mm at VF = 0.2.

For 1 sphere at VF = 0.2, $D = 11.62$ mm; 16 spheres at VF = 0.2, $D = 4.61$ mm.

For the case of spheres and ellipses at VF = 0.1: $D = 4.6$ mm/$a = 5.36$ $b = c = 4.288$ mm.

4.3. *Compression testing of cubes with multiple inclusions*

Compression testing was performed on the cases listed in Table 3 in accordance with ASTM D695-10 Standard Test Method for Compressive Properties of Rigid Plastics. This test method covers the determination of the mechanical properties of unreinforced and reinforced rigid plastics when loaded in compression at relatively low uniform rates of straining or loading and when test specimens of standard shape are employed. Utilized was a Tinius Olsen Universal testing machine (UTM) using load cell of 10 KN with speed of testing of 1 mm/min. Compressive modulus of elasticity values were arrived at from the linear portion of the stress-strain curves. Figure 6 shows such load-stroke (left) and stress-strain (right) curves. This was done by selecting a point along the straight-line portions and dividing the compressive stress by the corresponding strain value. Young's modulus values are obtained experimentally from results reported for all 36 cases and were calculated for all points after 1000 N at the linear part of the curve since before 1000 N recordings correspond to aligning the upper plate grip with the horizontal surface of the cubes this is why those points were disregarded and after 1000 N the alignment of both surfaces was perfect and this is where the modulus of elasticity was calculated. Each experiment was repeated 3 times by printing and testing these 3 different case cubes. Test results obtained from compression tests were almost identical for the same test case and the values reported below are the corresponding average values.

5. FEM of domain cubes containing multiple inclusions

This section reports on the details and results of the FEM simulations that are run along with the experimental cases tested in the previous Section. Discussed first is finite element simulations description followed by results of the FEM.

5.1. *FEM model*

All cases listed in Table 3 are modeled with FEM. The same *.stl files generated using Cubify Design® software used for 3D printing are used as computer-aided design (CAD) input files imported into the FEM software. The mechanical properties assigned to the defined cube are elastic and isotropic. For the matrix, the strength was tested in compression mode for multiple

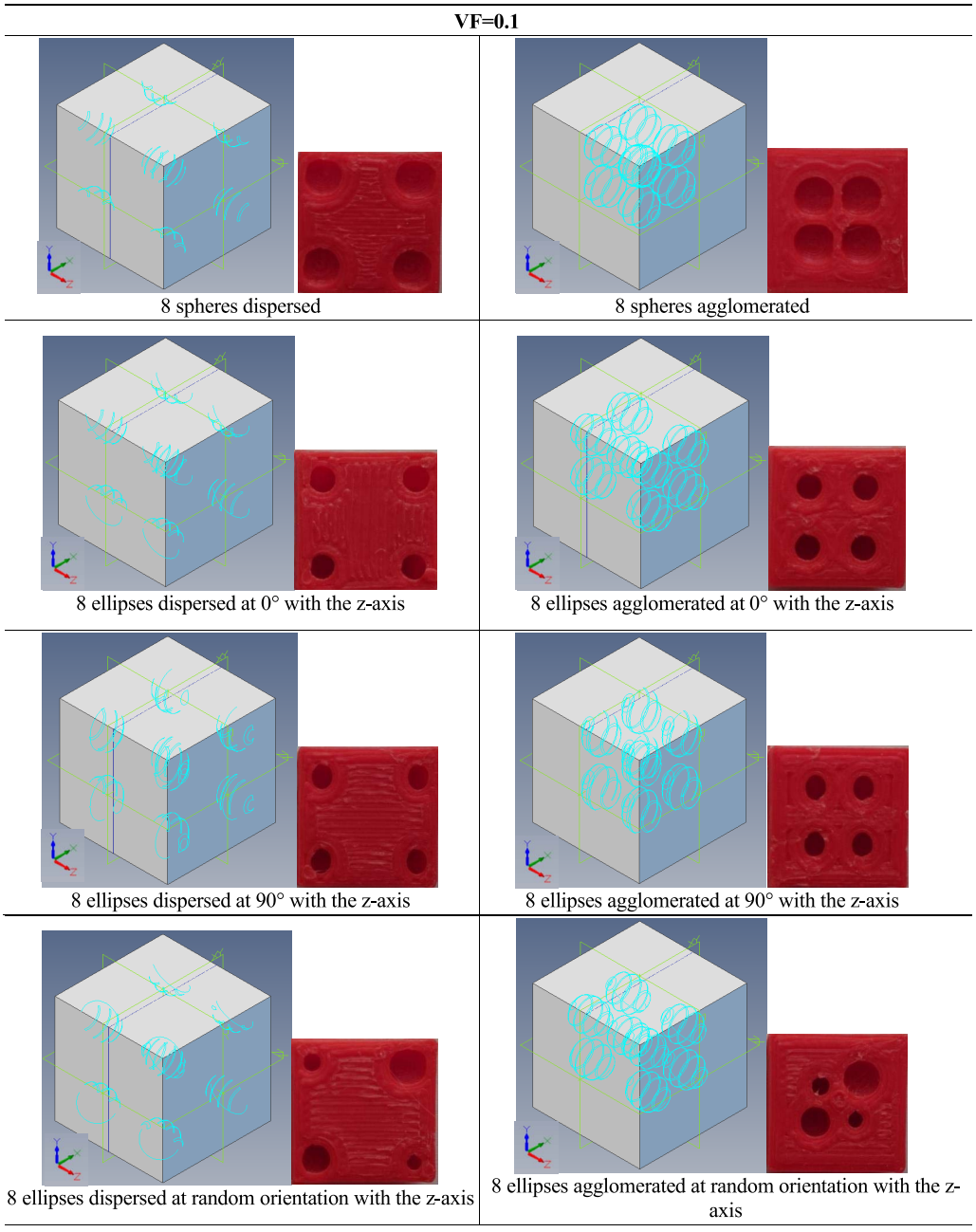

Figure 5. Continued on next page.

solid cubes (no inclusions) along the principal directions 1, 2, and 3. The results varied within a range of ±5% which suggests that the matrix is isotropic. An average of the measured modulus values in the three directions has been considered and the ABS printed compressive modulus was found to be 0.398 GPa and its Poisson's ratio of 0.35. This modulus value is significantly lower than reported moduli of solid ABS (typically 2.2 GPa) or that reported for other printed

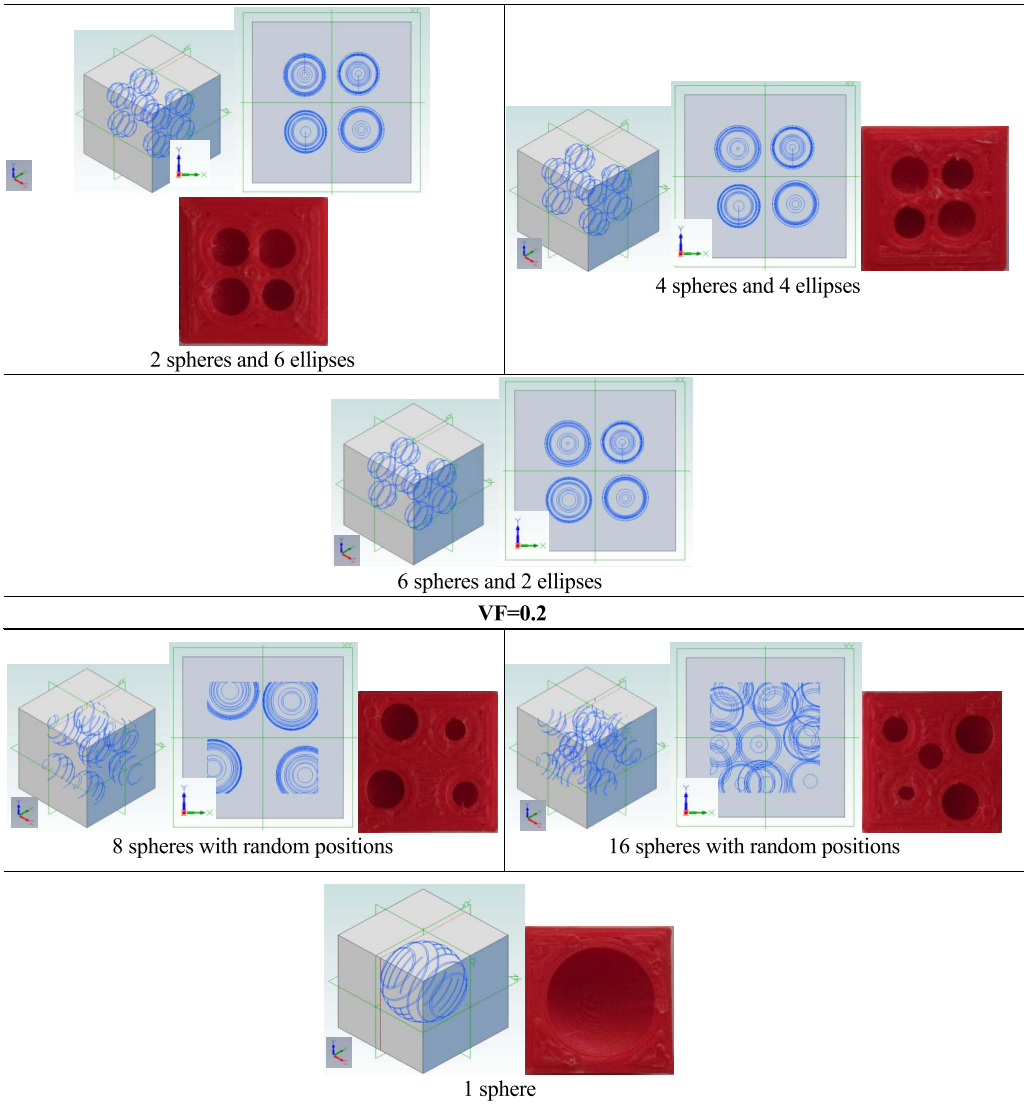

Figure 5 (cont.). Composites cases with different inclusion's orientation, distribution in the matrix, number and shape: 8 spheres dispersed, 8 spheres agglomerated, 8 ellipses dispersed at 0° with z-axis, 8 ellipses agglomerated at 0° with z-axis, 8 ellipses dispersed at 90° with z-axis, 8 ellipses agglomerated at 90° with z-axis, 8 ellipses dispersed at random orientation with z-axis, 8 ellipses agglomerated at random orientation with z-axis, 2 spheres and 6 ellipses, 4 spheres and 4 ellipses, 6 spheres and 2 ellipses, 1 sphere at VF = 0.2, 8 spheres at VF = 0.2 with random positions, 16 spheres at VF = 0.2 with random positions. Photographs of cross sections of the 3D printed cases are shown under each case.

ABS (of 1.5 GPa in Weiss, [20]). No apparent reason for this obvious disparity but given the wide variation in printer vendors and materials, it is possible that the proprietary filament was an ABS blend with lower stiffness or that the fusion process has negatively affected the final mechanical properties. Inclusions are set as voids thus $E_i = 0$ GPa and $\nu_i = 0$.

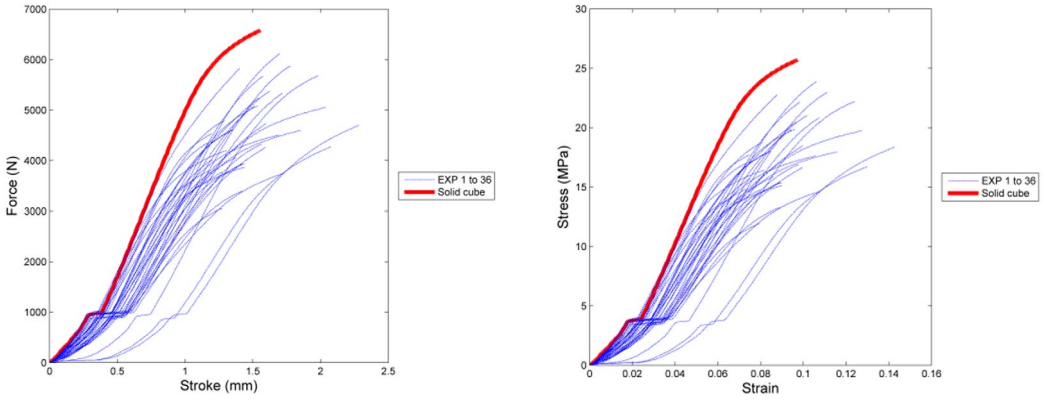

Figure 6. Compression tests: (left) force (N) versus stroke (mm) and (right) stress (MPa) versus strain curves of compression tests for 36 domain cubes (and 1 solid cube).

5.2. *Meshing, simulation control, and boundary conditions*

The commercially available DEFORM® 3D version 11 software package (from SFTC) was used. Tetrahedral elements are used to mesh the cube. Finer mesh is set at the top surface resulting in 130,000 elements. Active re-meshing is considered with relative interference ratio of 0.7. The time step is set at 0.001 s/step based on the smallest element size and the displacement rate as recommended by the software guidelines. Boundary conditions (BCs) are set so that $-z(-1)$ surface of the cube has displacement $uz = 0$; $+z(+1)$ surface has velocity displacement BC of 1.3 mm/min to mimic the upper rigid plate motion during uniaxial compression test. A heat transfer condition for all surfaces with the environment is set.

5.3. *FEM results*

Load versus stroke curves are used in FEM to determine the elastic Young's modulus for all cases considered. Figure 7 plots the results for the following 4 representative cases:

(a) solid cube,
(b) case 1: cube with dispersed 8 spheres at VF = 0.1, AR = 1, angle = 0°,
(c) case 2: cube with dispersed 8 ellipses at VF = 0.1, AR = 1.25, angle = 0°,
(d) case 3: cube with dispersed 8 ellipses at VF = 0.1, AR = 1.25, angle = 90°.

6. Results and discussion

The effective stiffness tensors are determined numerically for all cases using the developed homogenization methodology. The Young's modulus values normalized with respect to that of the matrix (E_{11}/E_m) from (4) are plotted versus volume fraction (VF) and location, average aspect ratio (AR), orientation, and number of inclusions. Overlaid when available, are experimentally and FEM-obtained stiffness values for those cases.

6.1. *Normalized longitudinal Young's modulus versus volume fraction (and location/ agglomeration)*

Figure 8 shows the normalized axial Young's modulus (with respect to that of the matrix) E_{11}/E_m plotted versus volume fraction for several and different methods and techniques, FEM: DEFORM® results, EXP: experimental results, NUM: numerical results using the developed

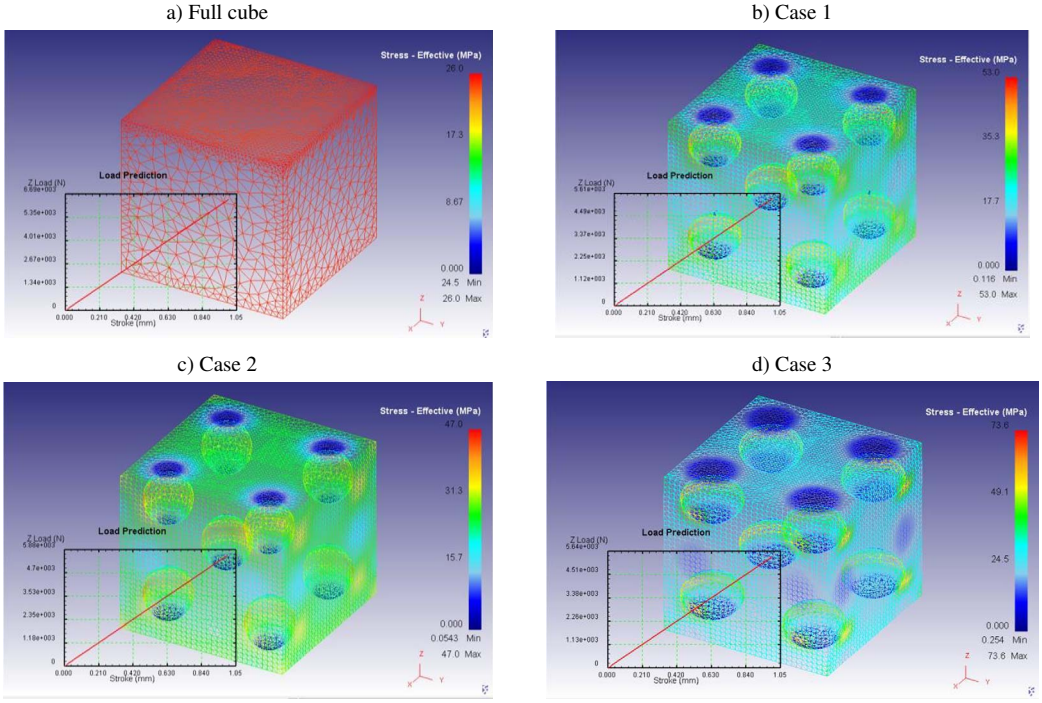

Figure 7. Load versus stroke obtained using FEM for (a) the solid cube, (b) case 1: cube with dispersed 8 spheres at VF = 0.1, AR = 1, angle = 0°, (c) case 2: cube with dispersed 8 ellipses at VF = 0.1, AR = 1.25, angle = 0°, (d) case 3: cube with dispersed 8 ellipses at VF = 0.1, AR = 1.25, angle = 90°.

homogenization work in this work, VUL: Voigt upper limit (Voigt [21]), and HSLL: Hashin-Shtrikman lower limit (Hashin and Shtrikman [22]). Figure 8 contains data points and fit lines corresponding to these 4 cases:

- 8 spheres dispersed
- 8 spheres agglomerated
- 8 ellipses dispersed at 0°
- 8 ellipses agglomerated at 0°

Results suggest that the stiffness calculated values from this homogenization methodology yield good agreement between numerical, experimental, and FEM results. The effective stiffness values of the composite depend strongly on the inclusions' volume fraction. Results of the normalized Young's modulus shows that E_{11}/E_m decreased with increased volume fraction for all cases considered. These results are in congruence with results reported by Xu *et al.* [23] where the predicted elastic moduli of particulate cementitious composite decreased with the fraction of voids of microencapsulated phase change materials (MPCMs) and increased with the fraction of quartz grains (hard inclusions). As the fraction of hard inclusions increase, the effective moduli would increase. Chen *et al.* [24] found that the elasticity of shale rock decreases with increasing volume fraction of multi-inclusions (as voids have a null modulus compared to the matrix similar to the case studied in this work) that is similar to the results found herein. However, their results are the inverse of those found in Xu *et al.* [25] since the inclusions are now harder than the matrix. The normalized effective Young's moduli of polymer nanocomposites increased with hard interfaces having modulus of elasticity larger than that of the matrix by 12 times.

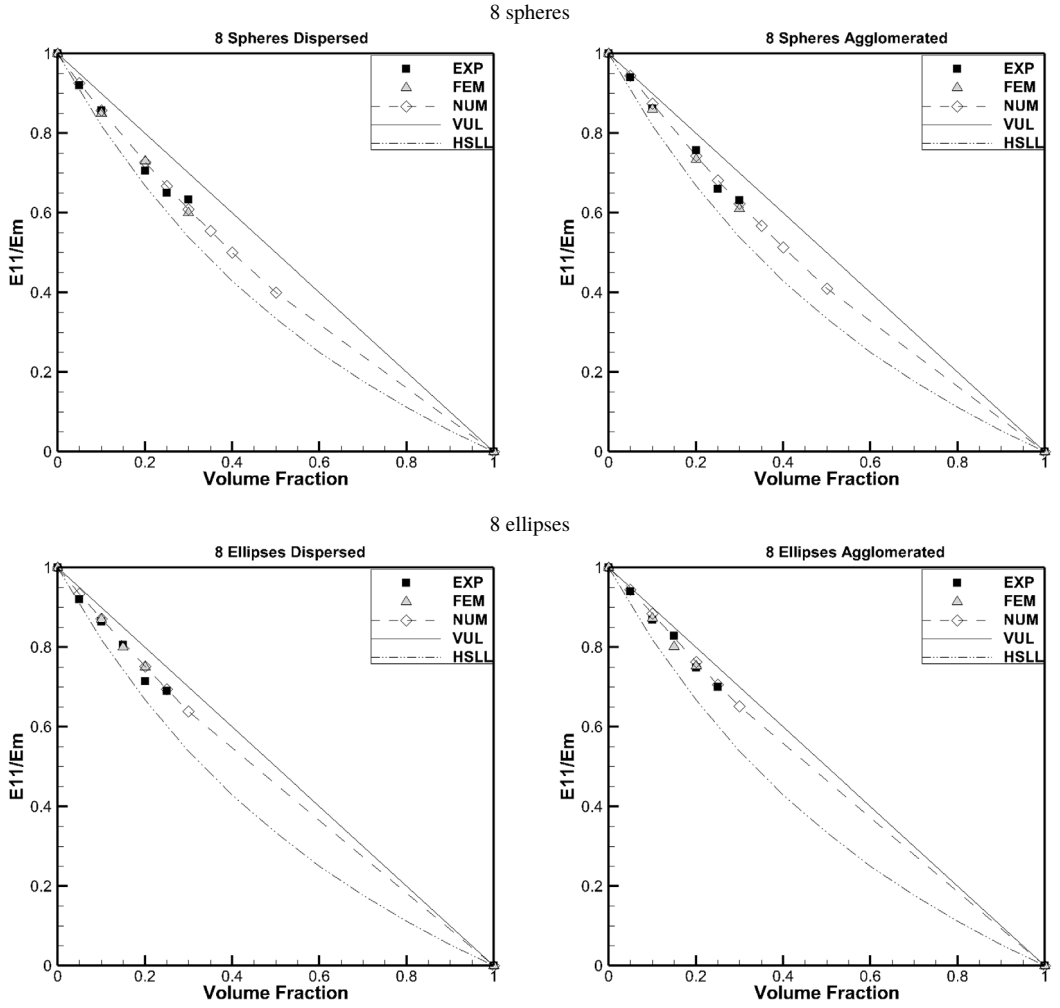

Figure 8. Normalized axial Young's modulus versus volume fraction for cases of 8 spheres dispersed and agglomerated, as well as 8 ellipses dispersed and agglomerated at 0° (EXP: experimental results, FEM: DEFORM® results, NUM: numerical results using the homogenization developed in this work, VUL: Voigt upper limit, HSLL: Hashin-Shtrikman lower limit).

Results also suggest that clustering of inclusions versus them being dispersed have little effect on the axial Young's modulus E_{11}/E_m. The difference between stiffness of spherical or elliptical inclusions whether dispersed or agglomerated is relatively insignificant and is estimated at about 2% only.

6.2. *Normalized longitudinal Young's modulus versus Aspect ratio*

Figure 9 shows the normalized axial Young's modulus E_{11}/E_m versus (a) percentage of spherical inclusions and (b) average aspect ratio for the below listed cases (EXP: experimental results, NUM: numerical results of this work, FEM: finite element) where all are at volume fractions = 0.1 and 0.2:

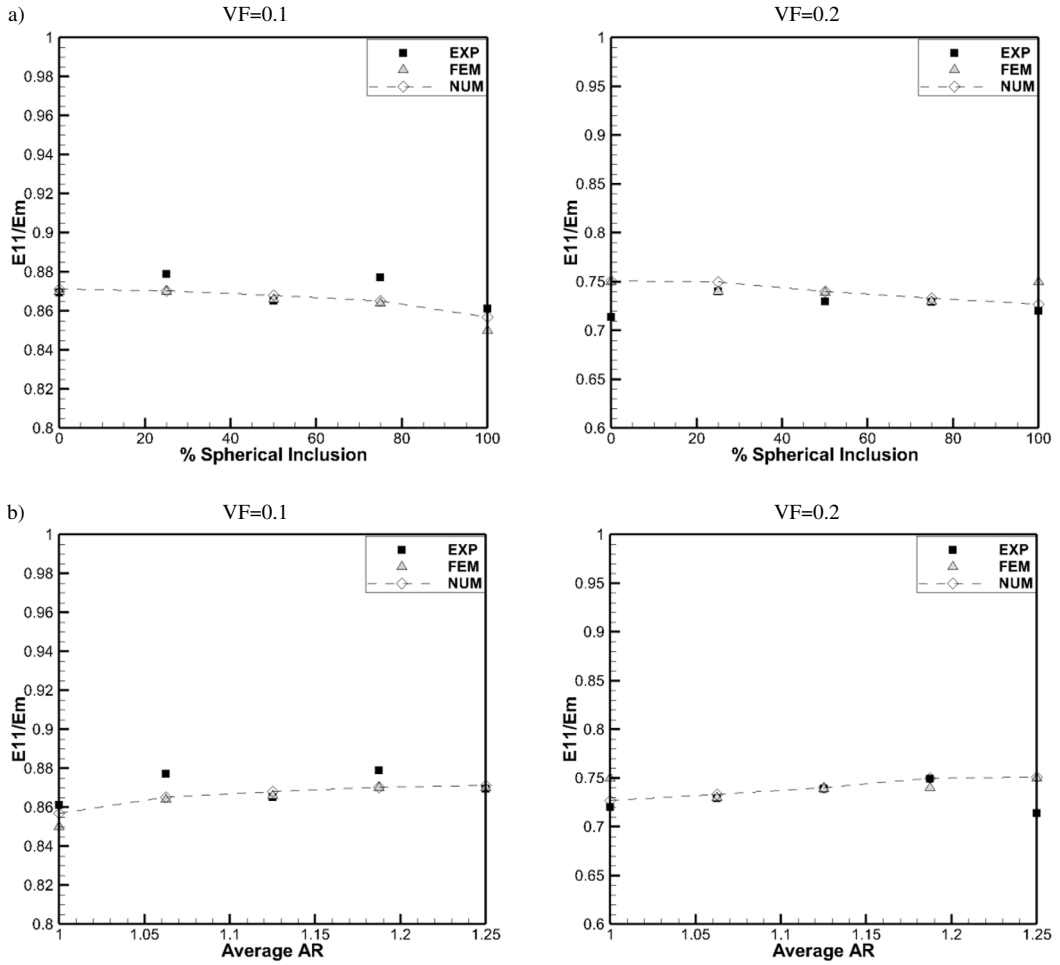

Figure 9. Plots of (a) normalized axial Young's modulus versus percentage spherical inclusions at VF = 0.1 and 0.2, (b) normalized axial Young's modulus versus average aspect ratio, AR at VF = 0.1 and 0.2 (EXP: experimental compression data, NUM: numerical solutions of the homogenization developed in this work, FEM: finite element).

- 0 spherical inclusions and 8 elliptical inclusions (0% percentage circular, average AR = 1.25)
- 2 spherical inclusions and 6 elliptical inclusions (25% percentage circular, average AR = 1.1875)
- 4 spherical inclusions and 4 elliptical inclusions (50% percentage circular, average AR = 1.125)
- 6 spherical inclusions and 2 elliptical inclusions (75% percentage circular, average AR = 1.0625)
- 8 spherical inclusions and 0 elliptical inclusions (100% percentage circular, average AR = 1).

Given the anemic trends in Figures 9(a) and 7(b), no solid conclusions can be drawn from within the range of the investigated aspect ratios to derive affirmative trends on the effect of the inclusions' average aspect ratio on stiffness or inversely versus % spherical inclusions (note

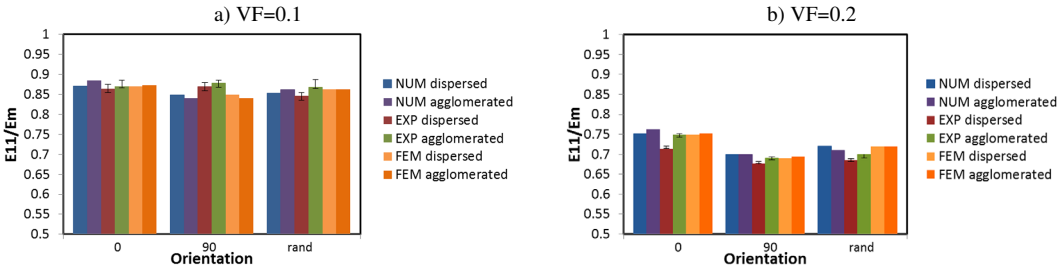

Figure 10. Normalized axial Young's modulus versus orientation for 0°, 90°, and random orientations at VF = 0.1 and 0.2 (EXP: experimental results, NUM: numerical results from this work, FEM: finite element method).

that higher AR values imply rounder or more spherical inclusions). It could also be inferred that normalized modulus exhibits slightly decreasing trend the more the inclusions are circular by 1.676% (at VF = 0.1) and 3.3084% (at VF = 0.2).

6.3. *Normalized longitudinal Young's modulus versus orientation (and location/agglomeration)*

As orientation is redundant in the case of spherical inclusions, the orientation of other shapes (here elliptical) is investigated as for their effect on the stiffness of the composite. Figure 10 shows results for the normalized axial Young's modulus E_{11}/E_m versus orientation for ellipses having AR = 1.25 at orientations of 0°, 90° and random, RAND VF = 0.1 and VF = 0.2. At such a value of aspect ratio, the effect of orientation is noticeable. Plotted, for all orientations, are results for experimental results, EXP, finite element FEM and numerical solution from (4), NUM. For the experimental results, shown in Figure 10 are error bars with respect to the arithmetic mean of the tests done for each case using the t-student distribution at a 95% confidence interval.

Analytical, finite element method, and experimental stiffness results show the difference between elliptical inclusions oriented at 0° with respect to the axial axis x1 and inclusions oriented at 90° with respect to the axial axis x1 is relatively significant with about 4.5% max relative difference recorded at AR = 1.25 (VF = 0.1) and 9.022% (VF = 0.2). Very good matches between experimental and numerical/FEM results are recorded. Observed variations (error bars) in the experimental results may be related to 3D printing of the tested cubes, UTM results, or human factors may affect the accuracy of experimental data. For the case of 8 ellipses dispersed, normalized Young's modulus values decreased by 2.17% in going from 8 ellipses oriented at 0° to random orientations (VF = 0.1), 4.14% (VF = 0.2), 1.53% for the case of 8 agglomerated ellipses (VF = 0.1) and by 6.96% (VF = 0.2). It can be inferred that the difference in orientations is more apparent at higher volume fractions.

6.4. *Normalized Young's modulus versus number of inclusions (and location/agglomeration)*

Figure 11 shows the normalized axial Young's modulus E_{11}/E_m versus number of spherical inclusions for the below listed cases (EXP: experimental results, NUM: numerical results of (4), FEM: finite element method):

- 1 spherical inclusion D = 11.62 mm at VF = 0.2 (analytical and experimental)
- 4 spherical inclusions D = 7.3 mm at VF = 0.2 (analytical)

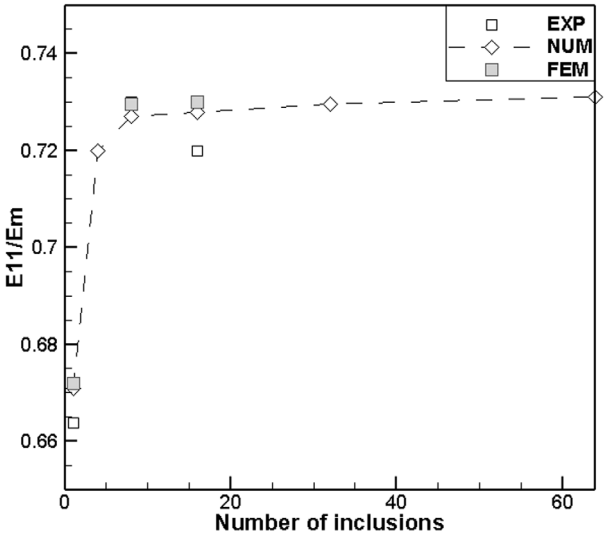

Figure 11. Normalized axial Young's modulus versus number of spherical inclusions (EXP: experimental results, NUM: numerical results using the homogenization developed in this work, FEM: finite element).

- 8 spherical inclusions $D = 5.8$ mm at VF = 0.2 (analytical and experimental)
- 16 spherical inclusions $D = 4.61$ mm at VF = 0.2 (analytical and experimental)

It can be inferred that E_{11}/E_m values increase with respect to number of spherical inclusions up to N of about 10. From $N = 1$ to $N = 1$, E_{11}/E_m values increased by 8.46%. For larger number of pores, this effect dwindles significantly. This is in agreement with Ju and Sun [12] and with Xu *et al.* [26] when the number of particles is greater than 49, the average value of elastic moduli of particle-reinforced composites PRCs particles tend to be stable) containing nonspherical. As the number of inclusions increases, their size would decrease for the same volume fraction. To ensure that all of the inclusions are bound within the RVE, investigated only is the case of clustered inclusions (agglomerated) near the RVE center.

6.5. *Normalized Young's modulus versus dispersion/agglomeration*

Some of the data reported in Figure 8 is re-examined here with focus on agglomeration and plotted as bar charts. For the below listed cases, Figure 12 (VF = 0 and VF = 1 not shown) shows the normalized axial Young's modulus E_{11}/E_m numerical values found from (4) for both dispersed and agglomerated cases:

- 8 spheres dispersed (Figure 12a)
- 8 spheres agglomerated (Figure 12a)
- 8 ellipses dispersed oriented at 0° (Figure 12b)
- 8 ellipses agglomerated oriented at 0° (Figure 12b).

It can be inferred that location has little effect on the modulus where maximum percentage difference recorded is about 2% for the range of volume fractions examined. This may be due to the small size of the RVE considered where the location of the inclusions does not appear to significantly affect the elastic properties of the composite.

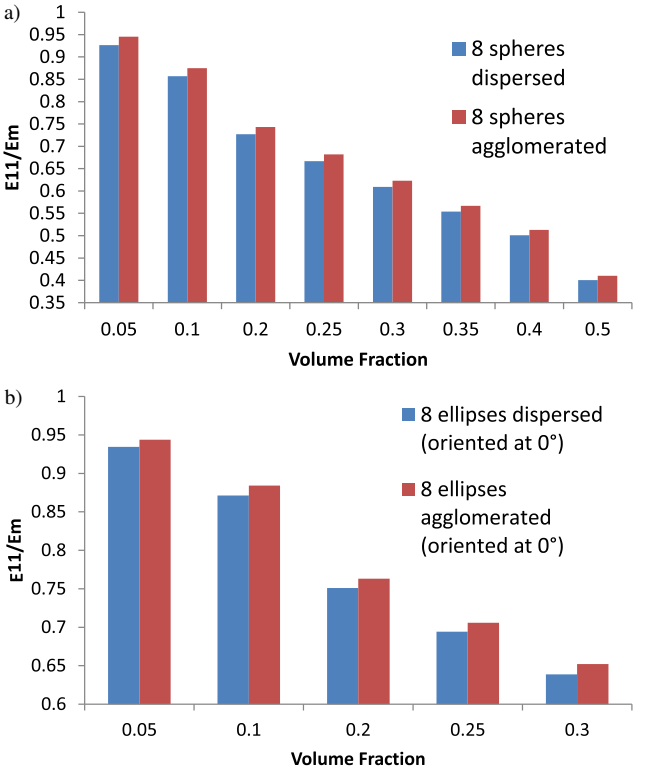

Figure 12. Normalized axial Young's modulus dispersed versus agglomerated for the numerical results (a) for 8 spheres and (b) for 8 ellipses oriented a 0°.

6.6. *Significance of the findings*

For all 36 cases tested experimentally, the normalized stiffness values determined from the numerical solution of (4) are plotted in Figure 13 against the experimentally measured normalized values. These Young's modulus values are determined at identical states of volume fractions, orientations, aspect ratios, locations, and numbers of inclusions. The figure shows a cloud of points, segregated by volume fraction values of 0.1, 0.15, 0.2, and 0.3, located close to the $y = x$ line which shows that experimental and numerical results are quite comparable. This is indicative of the quality of the formulations advanced in this work.

7. Conclusions

The generalized stiffness formulation (GSF) scheme is a combined expression (4) for the effective stiffness tensor of a multiple-inclusion composite. Inclusions states have five geometric and other attributes of volume fraction (size), shape, orientation, location, and number within the solid matrix. The formulation is first validated by comparing its numerical solutions with two literature-reported stiffness values of relatively simple configurations. With a DOE-developed test matrix accounting for wide-ranging values of these attributes, this formulation is further validated for a wide range of multiple inclusions composites using experimental compression tests and FEM simulations.

Examining the values of normalized axial modulus E_{11}/E_m versus the 5 inclusions' attributes, the following conclusions are drawn:

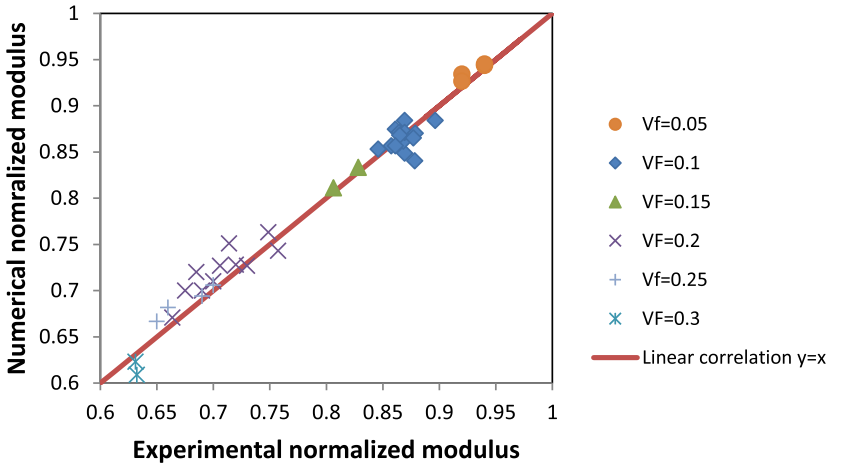

Figure 13. Plot of the numerical estimate of the Young's Modulus values produced in this work versus experimentally measured Young's Modulus values from compression tests.

- Volume fraction of inclusions in matrix (porosity, %) is very significant. E_{11}/E_m values decrease (increase) significantly for increasing (decreasing) porosity.
- Average aspect ratio, AR (circularity) of the inclusions. Trends of E_{11}/E_m with % circular inclusions (average aspect ratio) are inconclusive to make a definitive determination on their effect on composite stiffness. A slight decreasing trend of the modulus is shown with increasing number of spherical inclusions.
- Orientation of the inclusions is fairly significant in its effect on E_{11}/E_m. For the case of 8 ellipses dispersed, normalized Young's modulus values decreased by 2.17% in going from 8 ellipses oriented at 0° to random orientations and by 1.53% for the case of 8 agglomerated ellipses at VF = 0.1, 4.14% at VF = 0.2, 1.53% for the case of 8 agglomerated ellipses at VF = 0.1, and 6.96% at VF = 0.2. It can be inferred as well that the difference in orientations is more pronounce at higher volume fractions.
- Number of inclusions is significant (up to a point). The normalized axial effective Young's modulus E_{11}/E_m increases with the number of circular inclusions up to N = about 10 after which the effect is minimal. For the same volume fraction, as the number of inclusions increases their size would decrease. Therefore, in order to ensure that all of the inclusions are bound within the RVE, the case of the inclusions clustered near the center of the RVE is investigated.
- Location of the inclusions in the matrix (agglomerated versus dispersed) appears to have little effect (4.306%) on the normalized axial modulus E_{11}/E_m.

Acknowledgements

This work is made possible by the financial support of the Lebanese National Council for Scientific Research (CNRS) Award Number 103087. The authors also wish to acknowledge the support of the University Research Board at AUB.

References

[1] J. D. Eshelby, "The determination of the elastic field of an ellipsoidal inclusion, and related problems", *Proc. R. Soc. Lond. A* **241** (1957), p. 376-396.

[2] T. Mori, K. Tanaka, "Average stress in matrix and average elastic energy of materials with misfitting inclusions", *Acta Metall.* **21** (1973), p. 571-574.
[3] G. P. Tandon, G. J. Weng, "The effect of aspect ratio of inclusions on the elastic properties of unidirectionally aligned composites", *Polym. Compos.* **5** (1984), p. 327-333.
[4] E. Marklund, J. Varna, R. C. Neagu, E. K. Gamstedt, "Stiffness of aligned wood fiber composites: effect of microstructure and phase properties", *J. Compos. Mater.* **42** (2008), p. 2377-2405.
[5] V. Buryachenko, in *Micromechanics of Heterogeneous Materials*, Springer Science & Business Media, 2007.
[6] A. L. Kalamkarov, I. V. Andrianov, V. V. Danishevsâ, "Asymptotic homogenization of composite materials and structures", *Appl. Mech. Rev.* **62** (2009), 30802.
[7] W. J. Parnell, M. B. Vu, Q. Grimal, S. Naili, "Analytical methods to determine the effective mesoscopic and macroscopic elastic properties of cortical bone", *Biomech. Model. Mechanobiol.* **11** (2012), p. 883-901.
[8] H. M. Ma, X. L. Gao, "A new homogenization method based on a simplified strain gradient elasticity theory", *Acta Mech.* **225** (2014), p. 1075-1091.
[9] I. Hage, R. F. Hamade, "An experimentally validated combined stiffness formulation for a finite domain considering volume fraction, shape, orientation, and location of a single inclusion", *Int. J. Appl. Mech.* **10** (2018), 1850011.
[10] S. Li, G. Wang, R. A. Sauer, "The Eshelby tensors in a finite spherical domain—Part II: applications to homogenization", *J. Appl. Mech.* **74** (2007), p. 784-797.
[11] J. W. Ju, L. Z. Sun, "A novel formulation for the exterior-point eshelby's tensor of an ellipsoidal inclusion", *J. Appl. Mech.* **66** (1999), p. 570-574.
[12] J. W. Ju, L. Z. Sun, "Effective elastoplastic behavior of metal matrix composites containing randomly located aligned spheroidal inhomogeneities. Part I: micromechanics-based formulation", *Int. J. Solids Struct.* **38** (2001), p. 183-201.
[13] L. Z. Sun, J. W. Ju, "Elastoplastic modeling of metal matrix composites containing randomly located and oriented spheroidal particles", *J. Appl. Mech.* **71** (2004), p. 774-785.
[14] H. Askari, H. M. Zbib, X. Sun, "Multiscale modeling of inclusions and precipitation hardening in metal matrix composites: application to advanced high-strength steels", *J. Nanomech. Micromech.* **3** (2012), p. 24-33.
[15] T. Mura, *Micromechanics of Defects in Solids*, Kluwer, 1987.
[16] C. G. Koay, "On the six-dimensional orthogonal tensor representation of the rotation in three dimensions: a simplified approach", *Mech. Mater.* **41** (2009), p. 951-953.
[17] W. L. Bond, "The mathematics of the physical properties of crystals", *Bell Syst. Tech. J.* **22** (1943), p. 1-72.
[18] L. H. Dai, Z. P. Huang, R. Wang, "Explicit expressions for bounds for the effective moduli of multi-phased composites by the generalized self-consistent method", *Compos. Sci. Technol.* **59** (1999), p. 1691-1699.
[19] Y. Benveniste, "A new approach to the application of Mori–Tanaka's theory in composite materials", *Mech. Mater.* **6** (1987), p. 147-157.
[20] Z. Duan, X. Wang, Q. Gao, L. Zhang, B. Liu, I. Kim, "Highly active bifunctional cobalt-salen complexes for the synthesis of poly(ester-block-carbonate) copolymer via terpolymerization of carbon dioxide, propylene oxide, and norbornene anhydride isomer: roles of anhydride conformation consideration", *J. Polym. Sci. A* **52** (2014), p. 789-795.
[21] W. Voigt, in *Theoretische studien über die elasticitätsverhältnisse der krystalle*, Königliche Gesellschaft der Wissenschaften zu Göttingen, 1887.
[22] Z. Hashin, S. Shtrikman, "A variational approach to the theory of the elastic behaviour of multiphase materials", *J. Mech. Phys. Solids* **11** (1963), p. 127-140.
[23] W. Xu, M. Jia, Z. Zhu, M. Liu, D. Lei, X. Gou, "n-Phase micromechanical framework for the conductivity and elastic modulus of particulate composites: design to microencapsulated phase change materials (MPCMs)-cementitious composites", *Mater. Des.* **145** (2018), p. 108-115.
[24] Q. Chen, M. M. Nezhad, Q. Fisher, H. H. Zhu, "Multi-scale approach for modeling the transversely isotropic elastic properties of shale considering multi-inclusions and interfacial transition zone", *Int. J. Rock Mech. Min. Sci.* **84** (2016), p. 95-104.
[25] W. Xu, F. Wu, Y. Jiao, M. Liu, "A general micromechanical framework of effective moduli for the design of nonspherical nano-and micro-particle reinforced composites with interface properties", *Mater. Des.* **127** (2017), p. 162-172.
[26] W. Xu, B. Xu, F. Guo, "Elastic properties of particle-reinforced composites containing nonspherical particles of high packing density and interphase: DEM–FEM simulation and micromechanical theory", *Comput. Methods Appl. Mech. Eng.* **326** (2017), p. 122-143.